Elucidating the Micronuclear Functions in the Central Nervous System

January 2022

Sarasa Yano

Elucidating the Micronuclear Functions in the Central Nervous System

A Dissertation Submitted to

the Graduate School of Life and Environmental Sciences,

the University of Tsukuba

in Partial Fulfillment of the Requirements

for the Degree of Doctor of Philosophy in Science

(Doctoral Program in Biological Sciences)

Sarasa Yano

Table of contents

Chapter 1:

Development of a MATLAB-based program, CAMDi (Calculating Automatic Micronuclei Distinction), for three-dimensional quantitative analysis of micronuclei

1-1. Abstract

The micronucleus is known to be a biomarker for genomic instability. Normally, micronuclei are produced by segregation errors and mechanical stresses arising from dividing or migrating cells. The quantification of micronuclei is also widely used to test genotoxicity *in vitro*. While the micronuclei often emerge in damaged tissues, it is unable accurate counting micronuclei because the traditionally systems for counting micronuclei process the two- dimensional information. Here, I introduce a novel MATLAB-based program for quantifying micronuclei (CAMDi: Calculating Automatic Micronuclei Distinction) *in vitro* and *in vivo*. CAMDi is adaptable to various experimental imaging techniques and is useful for obtaining reproducible data. Using CAMDi, I revealed a novel link between the emergence of micronuclei and neuroinflammation. I found that administration of LPS into mice slightly increases micronuclei formation in the hippocampus region. On the other hand, direct stimulation of primary neuron did not increase the number of micronuclei, suggesting that the micronuclear formation is mediated through an intercellular communication associated with neuroinflammation. I provide a novel tool, CAMDi, to quantify micronuclei and demonstrate that neuroinflammation cause the production of micronuclei in the brain.

1-2. Introduction

Research on micronuclei in cancer cells has made marked progress. Micronuclei can also be observed in other tissues, including the brain. For instance, micronucleus is associated with neurodegenerative disorders and acts as a biomarker for them[23]. Since excess inflammation are known to cause DNA damage in tumor cells, neuroinflammation frequently observed in the neurodegenerative brain may also trigger micronucleus formation in the brain[24].

Several studies have reported approaches to quantify micronuclei *in vitro* and *in vivo*. The most common approach involves detecting the small nuclei by nuclear staining and counting them manually or automatically[9,25-28]. These standard approaches are employed to count the number of small nuclei by setting the threshold, such as the nuclear size. This approach is used to obtain data effectively and for general use. Quantification in conjunction with high-throughput screening and machine learning is powerful for analyzing the genomic condition *in vitro*[27,28].

Micronuclei can be stained the same way as regular nuclei and be discriminate from nuclei by their much smaller size. The traditional automatic systems for counting micronuclei have used images taken from just a single section. If it is taken near the top or bottom of the nucleus, the size of the cross-section would be much smaller than if the area near the center of the nucleus is selected. Since a cross-section close to the periphery of a nucleus can easily be mistaken for a micronucleus, it is technically difficult to define precise data on the micronucleus in tissues. Additionally, it is also difficult to distinguish the micronuclei from each nucleus when the nuclei are tightly packed in a limited area.

Therefore, the development of another application tool to quantify micronuclei precisely has been awaited.

I developed a MATLAB-based software, CAMDi. CAMDi is a useful program that quantifies the micronuclei precisely based on Z-stack position information. CAMDi can quantify micronuclei in both culture cells and thick tissue sections. Moreover, the CAMDi can distinguish the subcellular localization of micronuclei via triple staining and ellipse fitting functions even in dense conditions. Using CAMDi, I investigate the link between micronuclei formation and neuroinflammation. Although treatment with inflammatory cytokines induces neuroinflammation but has little effect on producing micronuclei in primary neurons, the administration of lipopolysaccharide (LPS) significantly induces micronuclei formation in the hippocampus region. These observations suggest that neuroinflammation promotes micronuclei formation.

1-3. Materials and methods

Cell cultures

Primary neurons were prepared from Crl:CD1(ICR) mice at embryonic day (E) 13.5-14.5 as previously described [29]. Briefly, mouse cortical neurons were plated on coverslips coated with 0.01875% Poly (ethylenimine) solution (SIGMA) and cultured in Neurobasal medium (Thermo Fisher Scientific) containing B-27 supplement (Thermo Fisher Scientific) and 100 units penicillin/100 mg streptomycin (P/S) (Thermo Fisher Scientific). Neurons were maintained for 4 days at 37℃ with 5% CO_2 and were then subjected to immunocytochemistry.

Immunocytochemistry

Primary neurons (4 days *in vitro*) were stimulated by either 1.0 μg/ml LPS (SIGMA), 50 ng/ml TNF-α (R&D Systems), or 5.0 μg/ml Polyinosinic-polycytidylic acid (Poly I:C) (SIGMA) for 24 hours and were then subjected to immunocytochemistry. Primary neurons were fixed with 4% paraformaldehyde (PFA) in phosphate-buffered saline (PBS) for 10 min at room temperature. Neurons on coverslips were blocked in 0.4% Triton X-100 in blocking solution (3% bovine serum albumin [BSA] in PBS) for 30 min at room temperature and then incubated with primary antibodies at 4℃ overnight. Anti-Lamin B1 (1:1000, Abcam, ab16048), anti-MAP2 (1:500, Merck Millipore, MAB378) antibodies were used. After washing with PBS, the cells were incubated with either anti-rabbit Alexa Fluor Plus 488 (1:500, Thermo Fisher Scientific) or anti-rabbit Dylight Fluorochome 488

(1:500, Abcam) conjugated secondary antibodies and anti-mouse Dylight Fluorochrome 594 (1:500, Abcam) conjugated secondary antibody diluted in blocking solution for 60 min at room temperature. Nuclei were stained with 10 μg/ml Hoechst 33342 (1:1000, Thermo Fisher Scientific). The coverslips were then mounted onto slides using FLUOROSHIELD Mounting Medium (ImmunoBioScience). Fluorescent images were obtained using a fluorescence microscope (BZ-9000, Keyence).

Immunohistochemistry

The C57BL/6 mice (2 months old) were injected with 1.0 mg/kg LPS (SIGMA) for 24 hours and were perfused with 4% PFA-PBS after anesthetizing with isoflurane. The brains were removed and fixed with the same fixative solution overnight. After 30% sucrose-PBS infiltration, the samples were embedded in Tissue-Tek Optical Cutting Temperature (O.C.T.) compound (SAKURA) and sliced at 30 μm thickness using the cryostat (Leica Biosystems). The tissue sections were blocked for 1 hour in 5% BSA in PBS and incubated with a primary antibody in 0.1% Triton X-100 in TBS (25 mM Tris-HCl [pH 7.5], 0.14 M NaCl) for either 1 day (anti-GFAP antibody) or 3 days (anti-MAP2 antibody) at 4°C. Anti-MAP2 (1:500, Merck Millipore, MAB378), and anti-GFAP (1:1000, SIGMA, G-A-5) antibodies were used. Following the wash with TBST, the tissue sections were incubated with an anti-mouse Dylight Fluorochrome 594 (abcam) secondary antibody diluted 1/500 in TBST together with 1.0 μg/ml DAPI (DOJINDO) for 1 hour at room temperature. The tissues were then mounted onto slides using VECTASHIELD Mounting Medium (Vector Laboratories). Tissue specimens were

observed using a confocal laser scanning microscope (LSM700, Carl Zeiss). All of the animal experiments were conducted according to the university guidelines for animal care and use. This study was approved by the Animal Experiment Committee in the University of Tsukuba (the approval numbers:19-340, 20-438, 21-443).

Micronuclei imaging

The C57BL/6 mice (2 months old) were anesthetized with isoflurane and perfused with 4% PFA-PBS. Each tissue (heart, skeletal muscle, kidney, spleen, thymus, testis) of mice was fixed with the same solution overnight. After 30% sucrose-PBS infiltration, the samples were embedded in Tissue-Tek O.C.T. compound (SAKURA) and sliced at a 30 μm thickness. The tissue sections were then incubated at 10 μg/ml Hoechst/TBST for 2 hours. Tissue specimens were observed using a confocal laser scanning fluorescence microscope (LSM700, Carl Zeiss).

Micronuclei analysis

FIJI ImageJ software (NIH) and ZEN (Carl Zeiss) were used for converting each Z-stack image (interval: 1 μm per image, total thickness: 10 - 15 μm) to a single TIFF file. The data were imported into MATLAB software, CAMDi, which can analyze three distinct colors (e.g., blue: nucleus/micronucleus; green: the marker for nucleus/micronuclei; red: cell markers). Quantifying the marker, such as Lamin B1, provides us information on the status of the nuclear envelope and chromatin conditions. The imported data were conducted binarization and the threshold of each color was determined. After making the

binary images, the merged areas were extracted according to the threshold and the number and area were quantified. The detailed flow for analyzing the micronuclei is described in the Results section. All data were reproduced in at least two independent experiments.

Statistical analysis

The statistical data were calculated by GraphPad Prism (GraphPad Software) and compared by Student's *t*-test and one-way analysis of variance (ANOVA).

1-4. Results

Micronuclei emerge in various tissues under normal conditions

Because the micronuclei emerge in various tissues in response to genotoxic stimulation[8], I investigated whether the micronuclei are observed in normal tissues, such as the heart, skeletal muscle, kidney, spleen, thymus, and testis. I found that some micronuclei exist in these tissues, even under normal conditions (Figure 1A and 1B). The occurrences of micronuclei in the spleen and kidney, which are highly proliferative, were much higher than those in the heart and muscles, which are composed of non-dividing cells, suggesting that formation of micronuclei may be related with cell proliferation. Next, I observed whether brains possess micronuclei. Since neurons are not dividing cells, I speculated that few micronuclei exist in the cerebral parenchyma. Interestingly, several micronuclei were observed in the cerebral cortex and hippocampus (Figure 1C and 1D). Because the brain is composed of both neurons and glia, it is likely that glial cells have micronuclei in the cerebral parenchyma. To investigate this idea, I observed specific regions in the cerebral cortex and hippocampus. Micronuclei exist in both $MAP2^+$ neurons and $GFAP^+$ astrocytes (Figure 2A and 2B), indicating that micronuclei appear in the brain ubiquitously. To summarize these observations, micronuclei exist in not only tumor tissues but also other tissues, including the brain, under normal conditions.

Developing the micronuclei analysis tool using the MATLAB-based program

Since the micronucleus is defined by several parameters, such as nuclear components and size, the precise quantification of micronuclei is challenging. Several methods to quantify

micronuclei have been reported to date[9,25-28]. The most frequently used method involves counting the small nuclei by analyzing the nuclear size as the index. This approach cannot, however, exclude the possibility that the regular nucleus is counted as a micronucleus when the edge of the nuclear section is identified using a confocal laser microscope (Figure 3A). To address this, I developed a micronuclei analysis program, CAMDi, to quantify the micronucleus precisely using MATLAB software. The conspicuous advantage of this CAMDi is that it can distinguish between micronuclei and regular nuclei. Sequential images with positional information are acquired using a confocal laser microscope. These images are stacked to a sequential image, divided into each color, converted into a single TIFF file containing three-dimensional information, and imported into CAMDi. Next, the number of micronuclei is analyzed based on three-dimensional image information (Figure 3B and 3C). CAMDi can also be utilized for not only three-dimensional but also two-dimensional images by changing the initial parameters. Furthermore, the CAMDi can define the micronuclear characteristic analyzed by nuclear components and cell-type specificity. The overall workflow for operating the CAMDi is illustrated in Figure 3D.

Processing flow of the MATLAB-based program, CAMDi

First, the initial parameters in the main program have to be defined. Information on each image, such as two-dimensional or three-dimensional, is inputted into CAMDi. Then, the parameter for the voxels, smoothing, and the radius of a nucleus is set in the "main" program through MATLAB windows (Table 1A). Next, the values to adjust the noise

reduction in the smoothing process are defined to convert the binarized images accurately (Table 1B). Distinct nuclei are divided using the ellipse fitting functions (Table 1C). The ellipse fitting is usually an optional function to analyze micronuclei.

1. Import each image to the CAMDi

Because the CAMDi program requires the TIFF images, it is necessary to convert the single or sequential images into TIFF images via the proper applications. Each image is imported through the "Import" windows (Figure 4A).

2a. Set each parameter (nuclear size)

CAMDi can distinguish between a small nucleus (micronucleus) and a large nucleus (regular nucleus in each cell). First, the radius of each nucleus is defined. The R_{cal} is a converted radius, which is calculated from the sequential images through the "main" program. In the case of three-dimensional analysis, R_{cal} is calculated from the volume after assuming that the nucleus is a sphere, whereas R_{cal} is calculated from the area after assuming that the nucleus is a circle in the two-dimensional analysis (Figure 4B). Each parameter is defined as follows. Min. radius (1) -> minimum radius of micronucleus, Max. radius (1) -> maximum radius of micronucleus, Min. radius (2) -> minimum radius of nucleus, Max. radius (2) -> maximum radius of nucleus.

2b. Set each parameter (overlap rate)

To analyze the characteristics of micronuclei, the rate of overlap area has to be calculated through the CAMDi windows or the "main" program. The default setting is 0.5, which represents 50% of the red area overlapped with the green or blue area. If a measurement value is higher than a set value, the nucleus is defined as an objective

nucleus. Using the pull-down window (i) in Figure 4C, non-overlapped nuclei with the red areas can also be counted.

2c. Set each parameter (threshold of each color)

The fluorescence intensities of each color (red, green, and blue) are adjusted. This flow is implemeted in the process of converting the binary image. CAMDi has two processes: the first is automatic processing, and the second is manual processing. In automatic processing, the value of sensitivity is adjusted. The sensitivity is utilized by a discriminant analysis method when the images are converted into binary images. In this step, the discriminant analysis is adaptively performed for each local area rather than for the whole image area. The window for manual processing emerges when the mark of "Adaptive threshold" is excluded. The threshold can be determined by altering the image frames (Figure 4D).

3. Binarization

After setting each parameter, the images are converted into binary images (Figure 4E). The binary images should be checked by eye to ensure they do not contain errors. Before the binarization, the images are executed by smoothing processing based on the bilateral filter. The bilateral filter is a smoothing filter that reduces noises in conjunction with preserving a part of the edges.

4. Minor adjustment

Using the function of "modify analyzed results", each binarized image is corrected to have proper data, such as separation, deletion, and merge (Figure 4F).

5. Clear border

The nuclei localized on the boundary of the x-z or y-z plane can be excluded after binarization when the "Clear border" box is checked. The nuclei on the x-y plane are not excluded (Figure 4G).

6. Analysis

Finally, the data are analyzed using the binary images, and the number of micronuclei is quantified and exported as csv, txt, and tiff files (Figure 4H).

7. Ellipse fitting (optional)

In the high-density area, it is difficult to quantify the number of micronuclei because each nucleus is fused after binarization. The "Ellipse fitting" function can convert the fused nuclei signals into clear ellipse shapes (Figure 4I). Although the merged nucleus can be separated using the "modify analyzed results" window individually, the ellipse fitting functions can be defined as an individual nucleus automatically.

Inflammatory stimulations have little effect on micronuclei formation in neurons *in vitro*

The mechanisms that underlie the micronuclei formation in the brain remain unknown. Using the two-dimensional mode of CAMDi program (prm.dim_cell_analyze = 2, prm.dim_cell_radius = 2), I analyzed the micronuclei in primary neurons. Interestingly, the micronuclei were occasionally observed not only in the cell soma but also in the proximal dendrites and were coated by MAP2, which is a binding protein of the dendritic microtubules (Figure 5A). These data suggest that the micronuclei are produced even under normal conditions despite their small number and that they redistribute from the

soma to the base of processes. Next, to investigate the link between neuroinflammation and neuronal micronuclei, I stimulated primary neurons with 1.0 μg/ml LPS, 5.0 μg/ml poly (I:C), and 50 ng/ml TNFα. Although the expression level of Toll-like receptors and TNF receptors in neurons is not high, neurons respond to these stimulations[30, 31]. However, treatments with these stimulations did not significantly increase the number of micronuclei in this system (Figure 5A and 5B), suggesting that these stimulations have little effect on micronuclei formation directly.

Inflammatory stimulation promotes micronuclei formation *in vivo*

It is well known that most cells in the brain are glia, such as astrocytes. Because of this, I tested if glia activated by inflammatory stimulation influences micronuclei formation in the cerebral cortex and hippocampus (Figure 6A and 6B). To investigate these regions, I administrated 1.0 μg/kg LPS into 8-week-old mice by i.p. injection and analyzed the brain sections by immunohistochemistry. The administration of LPS had a small effect on the activation of astrocytes in the cerebral cortex under this condition (Figure 6C and 6D). On the other hand, this stimulation clearly increased the number of reactive astrocytes in the hippocampus (Figure 6E and 6F), suggesting that LPS injection enhances neuroinflammation in a region-specific manner. Next, I examined whether LPS administration increases the number of neuronal micronuclei in the brain. To determine this, I quantified the number of micronuclei using the three-dimensional mode of CAMDi (prm.dim_cell_analyze = 3, prm.dim_cell_radius = 2) after 24 hours of LPS injections. Since micronuclei are frequently localized in the dendrites and soma (see Figure 5A), I

focused on the MAP2 positive regions. First, I observed the deep layer of the posterior parietal association area in the cerebral cortex. The LPS i.p. injection did not significantly increase micronuclei formation in the MAP2+ neurons of the cerebral cortex (Figure 6G and 6H). Next, I observed the micronuclei in the hippocampus since the number of reactive astrocytes was increased after LPS injection. To examine this, I focused on the CA1 region (see Figure 6B). Consistent with the selective neuroinflammation in hippocampus, the number of micronuclei in MAP2+ neurons was slightly increased in the hippocampus, indicating that the micronuclei formation induced by neuroinflammation is region-specific (Figure 6I and 6J). Next, I investigated whether inflammatory stimulation induces astrocytic micronuclei formation in these areas. The number of astrocytic micronuclei was moderately but not significantly increased in both the cerebral cortex and hippocampus (Figure 6K to 6N), indicating that LPS-induced micronuclei formation preferentially occurs in hippocampal neurons. Because the neuronal micronuclei are also localized in the pyramidal cell layer, although few in number, I examined whether micronuclei were increased in the pyramidal cell layer of the CA1 region. To do this, I used the ellipse fitting functions to count the large nuclei because it is extremely difficult to analyze them with three-dimensional information due to their high density (Figure 6O). The number of micronuclei in the pyramidal cell layer was not increased following LPS stimulation, indicating that neuroinflammatory stimulation induces neuronal micronuclei in the hippocampus (Figure 6P). Finally, I examined whether inflammatory stimulation promotes micronuclei formation in hippocampal neurons directly. To examine this, I treated primary hippocampal neurons

with LPS and quantified the micronuclei. As a result, I found that LPS stimulation had little effect on micronuclei formation in primary hippocampal neurons (Figure 6Q and 6R). Intriguingly, the number of micronuclei with nuclear envelopes is slightly decreased independently of LPS stimulation. These data suggest the production of micronuclei in hippocampal neuron is not directly induced by LPS stimulation. Then, one possibility is that micronucleus formation in neurons is caused by some secretory factors from astrocytes that respond to LPS stimulation. However, further studies are needed to confirm this hypothesis. Also, Lamin B1-negative micronuclei were observed in hippocampal neurons (Figure 6R). As the nuclear envelope sequesters chromatin from cytoplasmic protein such as cGAS, the retention time of the nuclear envelope plays an important role in regulating the positive feedback of neuroinflammation in the hippocampal region. Taken together, these data suggest that neuronal micronucleus is a potential mediator for amplifying the neuroinflammatory response in the brain.

1-5. Discussion

In this chapter, I developed a MATLAB-based program, CAMDi, for quantifying micronuclei. CAMDi is capable of analyzing the three-dimensional images and discriminating micronuclei from nuclei. This program can also detect the nucleus even in high-density areas. Using CAMDi, I revealed that neuroinflammation promotes neuronal micronuclei formation in the brain. I found that the inflammatory stimulation is not sufficient for inducing micronuclei in primary neurons. On the other hand, the neuronal micronuclei are increased following LPS administration *in vivo*, implying that the formation of neuronal micronuclei is not a cell-autonomous event. My findings demonstrate that micronuclei are amplifiers for the inflammatory cascade in the brain (Figure 7).

CAMDi provides a robust analysis of three-dimensional Z-stack images. In the micronuclei quantification to date, it is difficult to distinguish between the regular nucleus and the micronucleus using tissue images taken by a confocal laser microscope (see Figure 3A). CAMDi can integrate the Z-stack information, reconstitute the nucleus stereographically *in silico*, and distinguish the micronuclei from the regular nuclei. Each threshold, such as size and Z-stack intervals, needs to be determined before analyzing. CAMDi provides robust and reproducible results and avoids person-to-person variability. This program is also useful when the cell density in the region is high (e.g., in the stratum pyramidale in the hippocampus). CAMDi can elicit each nucleus using ellipse fitting functions and analyze the suitable size of nuclei from Z-stack images, showing an accurate number of both nuclei and micronuclei. Previously, several groups have reported

a high-throughput screening system for quantifying micronuclei in culture cells[9,25-28]. Although the precise quantification methods *in vivo* have not been developed, investigating micronuclei is crucial to evaluate the pathological condition in each tissue. CAMDi enables us to evaluate the precise size of micronuclei via Z-stack sequential images. Additional staining, such as Lamin B1, helps us to understand the micronuclei conditions and to discriminate the micronucleus from artificial signals. Thus, CAMDi is a powerful application that is capable of acquiring accurate information from each tissue in physiological and pathological conditions.

Using CAMDi, I found that neuroinflammation increases the number of micronuclei in a region-specific manner. Recently, it has been reported that micronuclei enhance the inflammatory response in cancer cells via the innate immune system, the cGAS-STING pathway. The nuclear envelope is disrupted after forming micronuclei and the double-strand DNA is exposed to the cytoplasm. This cytoplasmic DNA activates cGAS, which synthesizes cGAMP, leading to the activation of STING on the endoplasmic reticulum (ER)[32]. Thus, it is likely that the micronuclei regulate the inflammatory response. On the other hand, the mechanisms that underlie neuroinflammation-induced micronuclei formation have not yet been elucidated. To date, it has been demonstrated that nuclear LC3/Atg8 regulates micronuclei formation in response to oncogenic stress, and this is followed by degrading the nuclear lamina [14]. During this process, the oncogenic stress, such as Ras activation, promotes this cascade. In contrast, inhibition of the autophagic pathway leads to accumulation of micronuclei in tumor cells. Although the precise mechanisms of how the oncogenic stress and the

autophagic pathway regulates micronuclei formation have not been fully elucidated, it is plausible to consider that neuroinflammation affects these pathways.

Interestingly, I observed that micronuclei mainly increased not in the stratum pyramidale but in the stratum radiatum in the hippocampus region. Because micronuclei are frequently observed in the neuronal dendrites in primary neurons, they may redistribute from the soma to the processes in response to inflammatory stimulation. Another possibility is that micronuclei are produced in the early stage and are sustained in the neurons of the postnatal brain. My preliminary data suggest that neurons can form micronuclei when they pass through the narrow region (see **Chapter 2**). Because part of the hippocampus is a high-density region, the mechanical stress during cell migration could produce the micronuclei that maintain in the neuronal dendrite and resist from degradation. Why the micronuclei exist in the dendrites remains unknown. As the ER in neurons is also expanded to the dendrites and spines[33,34], micronuclei in the proximal dendrites could be crucial for activating the cGAS-STING cascade locally. Because the micronuclei and cGAS-STING pathway are involved in the neurodegeneration such as Alzheimer's disease (AD), Parkinson's disease (PD), and amyotrophic lateral sclerosis (ALS)[23,35,36], the micronuclei-cGAS-STING pathway is a potential candidate linked to these disorders. It is important to note that neuronal micronuclei are not induced by stimulation with LPS, TNFα, and poly (I:C) directly. On the other hand, the administration of LPS activates astrocytes and promotes neuronal micronuclei formation in the hippocampus region. As reactive astrocytes secrete a variety of proteins under stress

conditions[37], several factors released from astrocytes may affect neuronal micronuclei formation.

Overall, I developed a MATLAB-based program to analyze micronuclei in the three-dimensional images *in vivo.* I believe that the CAMDi will serve as a powerful tool to answer the interesting remaining questions regarding cellular motility, inflammation, and chromosomal instability. Moreover, my finding may shed light on the unclarified mechanisms linking neuroinflammation to cognitive impairments and neurodegeneration[38].

Acknowledgement

I would first like to thank to Dr. Fuminori Tsuruta for advice on experimental design. I thank the lab members for helpful discussions and technical supports. I am grateful to Dr. Tomoki Chiba, Dr. Yu Hayashi, Dr. Kyoichi Sawamura, and Dr. Ban Sato for helpful discussions. I also thank Dr. T. Nagata for suggestion and guidance for developing CAMDi by MATLAB. I also appreciate Dr. Tomomi Okajima who taught me experiments, gave me advice, and encouraged me and Hikari Kubotani, Kaito Akiyama, Rio Tsuchiya and Natsu Asami for kind supports of the experiment and the analysis. I also wish to thank Dr. Yusuke Kishi (Pharmacy, Tokyo University), Prof. Yukiko Gotoh (Pharmacy, Tokyo University), Dr. Takeshi Ichinohe (The institute medical science, Tokyo University), Dr. Kenichiro Kubo, Dr. Kanehiro Hayashi, and Prof. Kazunori Nakajima (Anatomy, Keio University) for providing the experimental material. I am grateful to Prof. Noboru Mizushima for giving the pMRX-IP-GFP-LC3-RFP-LC3ΔG plasmid. I thank Dr. Ayako Kitazawa and Ms. Yuko Jinzenji for their technical supports. Advice and comments given by Dr. Mineko Kengaku (iCeMS, Kyoto University) has been a great help in neuronal migration experiments. The mass spectrometry analysis was supported by "Nanotechnology Platform Project" operated by the Ministry of Education, Culture, Sports, Science and Technology (MEXT), Japan (No. JPMXP09S19NM0031). This work was supported by JSPS Research Fellowship for Young Scientists (19J20619). Finally, I would like to express my gratitude to my family members and to my friends for supporting me and encouraging me throughout my years of study in Tsukuba.

References

1 Howell, W. H. The New Morphological Element of the Blood. *Science* **3**, 46-48, doi:10.1126/science.ns-3.49.46 (1884).

2 Dawson, D. W. & Bury, H. P. The significance of Howell-Jolly bodies and giant metamyelocytes in marrow smears. *J Clin Pathol* **14**, 374-380, doi:10.1136/jcp.14.4.374 (1961).

3 Sears, D. A. & Udden, M. M. Howell-Jolly bodies: a brief historical review. *Am J Med Sci* **343**, 407-409, doi:10.1097/MAJ.0b013e31823020d1 (2012).

4 Luzhna, L., Kathiria, P. & Kovalchuk, O. Micronuclei in genotoxicity assessment: from genetics to epigenetics and beyond. *Front Genet* **4**, 131, doi:10.3389/fgene.2013.00131 (2013).

5 Krupina, K., Goginashvili, A. & Cleveland, D. W. Causes and consequences of micronuclei. *Curr Opin Cell Biol* **70**, 91-99, doi:10.1016/j.ceb.2021.01.004 (2021).

6 Miller, K. N., Dasgupta, N., Liu, T., Adams, P. D. & Vizioli, M. G. Cytoplasmic chromatin fragments-from mechanisms to therapeutic potential. *Elife* **10**, doi:10.7554/eLife.63728 (2021).

7 Jagetia, G. C. & Adiga, S. K. Correlation between micronuclei induction and cell survival in V79 cells exposed to paclitaxel (taxol) in conjunction with radiation. *Mutat Res* **377**, 105-113, doi:10.1016/s0027-5107(97)00067-5 (1997).

8 Morita, T., MacGregor, J. T. & Hayashi, M. Micronucleus assays in rodent tissues other than bone marrow. *Mutagenesis* **26**, 223-230, doi:10.1093/mutage/geq066 (2011).

9 Fenech, M. & Morley, A. A. Measurement of micronuclei in lymphocytes. *Mutat Res* **147**, 29-36, doi:10.1016/0165-1161(85)90015-9 (1985).

10 Watters, G. P., Smart, D. J., Harvey, J. S. & Austin, C. A. H2AX phosphorylation as a genotoxicity endpoint. *Mutat Res* **679**, 50-58, doi:10.1016/j.mrgentox.2009.07.007 (2009).

11 Wolf, K. *et al.* Physical limits of cell migration: control by ECM space and nuclear deformation and tuning by proteolysis and traction force. *J Cell Biol* **201**, 1069-1084, doi:10.1083/jcb.201210152 (2013).

12 Denais, C. M. *et al.* Nuclear envelope rupture and repair during cancer cell migration. *Science* **352**, 353-358, doi:10.1126/science.aad7297 (2016).

13 Raab, M. *et al.* ESCRT III repairs nuclear envelope ruptures during cell migration to limit DNA damage and cell death. *Science* **352**, 359-362, doi:10.1126/science.aad7611 (2016).

14 Dou, Z. *et al.* Autophagy mediates degradation of nuclear lamina. *Nature* **527**, 105-109, doi:10.1038/nature15548 (2015).

15 Mochida, K. *et al.* Receptor-mediated selective autophagy degrades the endoplasmic reticulum and the nucleus. *Nature* **522**, 359-362, doi:10.1038/nature14506 (2015).

16 Rello-Varona, S. *et al.* Autophagic removal of micronuclei. *Cell Cycle* **11**, 170-176, doi:10.4161/cc.11.1.18564 (2012).

17 Zink, D., Fischer, A. H. & Nickerson, J. A. Nuclear structure in cancer cells. *Nat Rev Cancer* **4**, 677-687, doi:10.1038/nrc1430 (2004).

18 Dou, Z. *et al.* Cytoplasmic chromatin triggers inflammation in senescence and cancer. *Nature* **550**, 402-406, doi:10.1038/nature24050 (2017).

19 Bakhoum, S. F. *et al.* Chromosomal instability drives metastasis through a cytosolic DNA response. *Nature* **553**, 467-472, doi:10.1038/nature25432 (2018).

20 Zhang, C. Z. et al. Chromothripsis from DNA damage in micronuclei. *Nature.* 522, 179-184, doi:10.1038/nature14493 (2015).

21 S. Yue. et al., Cell-type-specific role of lamin-B1 in thymus development and its inflammation-driven reduction in thymus aging. Aging Cell. 18(4), doi: 10.1111/acel.12952 (2019)

22 Amy H. Yang et al., Chromosome Segregation Defects Contribute to Aneuploidy in Normal Neural Progenitor Cells. *J Neuro Sci.* 23(32):10454 – 10462. (2003)

23 Migliore, L., Coppede, F., Fenech, M. & Thomas, P. Association of micronucleus frequency with neurodegenerative diseases. *Mutagenesis* **26**, 85-92, doi:10.1093/mutage/geq067 (2011).

24 Jaiswal, M., LaRusso, N. F., Burgart, L. J. & Gores, G. J. Inflammatory cytokines induce DNA damage and inhibit DNA repair in cholangiocarcinoma cells by a nitric oxide-dependent mechanism. *Cancer Res* **60**, 184-190 (2000).

25 Sommer, S., Buraczewska, I. & Kruszewski, M. Micronucleus Assay: The State of Art, and Future Directions. *Int J Mol Sci* **21**, doi:10.3390/ijms21041534 (2020).

26 Shibai-Ogata, A., Kakinuma, C., Hioki, T. & Kasahara, T. Evaluation of high-throughput screening for in vitro micronucleus test using fluorescence-based cell imaging. *Mutagenesis* **26**, 709-719, doi:10.1093/mutage/ger037 (2011).

27 Wilson, A. *et al.* Transforming early pharmaceutical assessment of genotoxicity: applying statistical learning to a high throughput, multi end point in vitro micronucleus assay. *Sci Rep* **11**, 2535, doi:10.1038/s41598-021-82115-5 (2021)

28 Shuryak, I. *et al.* Machine learning methodology for high throughput personalized neutron dose reconstruction in mixed neutron + photon exposures. *Sci Rep* **11**, 4022, doi:10.1038/s41598-021-83575-5 (2021)

29 Tsuruta, F., Okajima, T., Yano, S. & Chiba, T. Quantification of Endosome and Lysosome Motilities in Cultured Neurons Using Fluorescent Probes. *J Vis Exp*, doi:10.3791/55488 (2017).

30 Okun, E., Griffioen, K. J. & Mattson, M. P. Toll-like receptor signaling in neural plasticity and disease. *Trends Neurosci* **34**, 269-281, doi:10.1016/j.tins.2011.02.005 (2011).

31 Probert, L. TNF and its receptors in the CNS: The essential, the desirable and the deleterious effects. *Neuroscience* **302**, 2-22, doi:10.1016/j.neuroscience.2015.06.038 (2015).

32 Ablasser, A. & Chen, Z. J. cGAS in action: Expanding roles in immunity and inflammation. *Science* **363**, doi:10.1126/science.aat8657 (2019).

33 Cui-Wang, T. *et al.* Local zones of endoplasmic reticulum complexity confine cargo in neuronal dendrites. *Cell* **148**, 309-321, doi:10.1016/j.cell.2011.11.056 (2012).

34 Spacek, J. & Harris, K. M. Three-dimensional organization of smooth endoplasmic reticulum in hippocampal CA1 dendrites and dendritic spines of the immature and mature rat. *J Neurosci* **17**, 190-203 (1997).

35 Paul, B. D., Snyder, S. H. & Bohr, V. A. Signaling by cGAS-STING in Neurodegeneration, Neuroinflammation, and Aging. *Trends Neurosci* **44**, 83-96, doi:10.1016/j.tins.2020.10.008 (2021).

36 Yu, C. H. *et al.* TDP-43 Triggers Mitochondrial DNA Release via mPTP to Activate cGAS/STING in ALS. *Cell* **183**, 636-649 e618, doi:10.1016/j.cell.2020.09.020 (2020).

37 Smith, H. L. *et al.* Astrocyte Unfolded Protein Response Induces a Specific Reactivity State that Causes Non-Cell-Autonomous Neuronal Degeneration. *Neuron* **105**, 855-866 e855, doi:10.1016/j.neuron.2019.12.014 (2020).

38 Zhao, J. *et al.* Neuroinflammation induced by lipopolysaccharide causes cognitive impairment in mice. *Sci Rep* **9**, 5790, doi:10.1038/s41598-019-42286-8 (2019).

39 Li, Q. & Barres, B. A. Microglia and macrophages in brain homeostasis and disease. *Nat Rev Immunol* **18**, 225-242, doi:10.1038/nri.2017.125 (2018).

40 Wolf, S. A., Boddeke, H. W. & Kettenmann, H. Microglia in Physiology and Disease. *Annu Rev Physiol* **79**, 619-643, doi:10.1146/annurev-physiol-022516-034406 (2017).

41 Masuda, T., Sankowski, R., Staszewski, O. & Prinz, M. Microglia Heterogeneity in the Single-Cell Era. *Cell Rep* **30**, 1271-1281, doi:10.1016/j.celrep.2020.01.010 (2020).

42 Keren-Shaul, H. *et al.* A Unique Microglia Type Associated with Restricting Development of Alzheimer's Disease. *Cell* **169**, 1276-1290 e1217, doi:10.1016/j.cell.2017.05.018 (2017).

43 M. van der Poel, M. *et al.* Transcriptional profiling of human microglia reveals grey-white matter heterogeneity and multiple sclerosis-associated changes. *Nat Commun* **10**, 1139, doi:10.1038/s41467-019-08976-7 (2019).

44 Nimmerjahn, A., Kirchhoff, F. & Helmchen, F. Resting microglial cells are highly dynamic surveillants of brain parenchyma in vivo. *Science* **308**, 1314-1318, doi:10.1126/science.1110647 (2005).

45 Haynes, S. E. *et al.* The P2Y12 receptor regulates microglial activation by extracellular nucleotides. *Nat Neurosci* **9**, 1512-1519, doi:10.1038/nn1805 (2006).

46 Wake, H., Moorhouse, A. J., Jinno, S., Kohsaka, S. & Nabekura, J. Resting microglia directly monitor the functional state of synapses in vivo and determine the fate of ischemic terminals. *J Neurosci* **29**, 3974-3980, doi:10.1523/JNEUROSCI.4363-08.2009 (2009).

47 Davalos, D. *et al.* ATP mediates rapid microglial response to local brain injury in vivo. *Nat Neurosci* **8**, 752-758, doi:10.1038/nn1472 (2005).

48 Cunningham, C. L., Martinez-Cerdeno, V. & Noctor, S. C. Microglia regulate the number of neural precursor cells in the developing cerebral cortex. *J Neurosci* **33**, 4216-4233, doi:10.1523/JNEUROSCI.3441-12.2013 (2013).

49 Perez-Pouchoulen, M., VanRyzin, J. W. & McCarthy, M. M. Morphological and Phagocytic Profile of Microglia in the Developing Rat Cerebellum. *eNeuro* **2**, doi:10.1523/ENEURO.0036-15.2015 (2015).

50 Block, M. L., Zecca, L. & Hong, J. S. Microglia-mediated neurotoxicity: uncovering the molecular mechanisms. *Nat Rev Neurosci* **8**, 57-69, doi:10.1038/nrn2038 (2007).

51 Crasta, K. *et al.* DNA breaks and chromosome pulverization from errors in mitosis. *Nature* **482**, 53-58, doi:10.1038/nature10802 (2012).

52 Shi, L., Qalieh, A., Lam, M. M., Keil, J. M. & Kwan, K. Y. Robust elimination of genome-damaged cells safeguards against brain somatic aneuploidy following Knl1 deletion. *Nat Commun* **10**, 2588, doi:10.1038/s41467-019-10411-w (2019).

53 Tabata, H. & Nakajima, K. Efficient in utero gene transfer system to the developing mouse brain using electroporation: visualization of neuronal migration in the developing cortex. *Neuroscience* 103, 865-872, doi:10.1016/s0306-4522(01)00016-1 (2001).

54 Komatsu, M. *et al.* Impairment of starvation-induced and constitutive autophagy in Atg7-deficient mice. *J Cell Biol* **169**, 425-434, doi:10.1083/jcb.200412022 (2005).

55 Mo, A. *et al.* Epigenomic Signatures of Neuronal Diversity in the Mammalian Brain. *Neuron* **86**, 1369-1384, doi:10.1016/j.neuron.2015.05.018 (2015).

56 Moriyama, M., Koshiba, T. & Ichinohe, T. Influenza A virus M2 protein triggers mitochondrial DNA-mediated antiviral immune responses. *Nat Commun* **10**, 4624, doi:10.1038/s41467-019-12632-5 (2019).

57 Goebbels, S. *et al.* Genetic targeting of principal neurons in neocortex and hippocampus of NEX-Cre mice. *Genesis* **44**, 611-621, doi:10.1002/dvg.20256 (2006).

58 Kim, J. *et al.* USP15 Deubiquitinates TUT1 Associated with RNA Metabolism and Maintains Cerebellar Homeostasis. *Mol Cell Biol* **40**, doi:10.1128/MCB.00098-20 (2020).

59 Tabata, H. & Nakajima, K. Labeling embryonic mouse central nervous system cells by in utero electroporation. *Dev Growth Differ* **50**, 507-511, doi:10.1111/j.1440-169X.2008.01043.x (2008).

60 Morrison, H., Young, K., Qureshi, M., Rowe, R. K. & Lifshitz, J. Quantitative microglia analyses reveal diverse morphologic responses in the rat cortex after diffuse brain injury. *Sci Rep* **7**, 13211, doi:10.1038/s41598-017-13581-z (2017).

61 Mure, K., Takeshita, T. & Morimoto, K. Categorization of micronuclei by size and measurement of each ratio in cytokinesis-block and conventional cultures of

human lymphocytes exposed to mitomycin C and colchicine. *Environ Health Prev Med* **1**, 93-99, doi:10.1007/BF02931197 (1996).

62 Sekine, K., Honda, T., Kawauchi, T., Kubo, K. & Nakajima, K. The outermost region of the developing cortical plate is crucial for both the switch of the radial migration mode and the Dab1-dependent "inside-out" lamination in the neocortex. *J Neurosci* **31**, 9426-9439, doi:10.1523/JNEUROSCI.0650-11.2011 (2011).

63 Kubo, K. *et al.* Ectopic Reelin induces neuronal aggregation with a normal birthdate-dependent "inside-out" alignment in the developing neocortex. *J Neurosci* **30**, 10953-10966, doi:10.1523/JNEUROSCI.0486-10.2010 (2010).

64 Kaizuka, T. *et al.* An Autophagic Flux Probe that Releases an Internal Control. *Mol Cell* **64**, 835-849, doi:10.1016/j.molcel.2016.09.037 (2016).

65 Chennakrishnaiah, S. *et al.* Extracellular vesicles from genetically unstable, oncogene-driven cancer cells trigger micronuclei formation in endothelial cells. *Sci Rep* **10**, 8532, doi:10.1038/s41598-020-65640-7 (2020).

66 Ginhoux, F., Lim, S., Hoeffel, G., Low, D. & Huber, T. Origin and differentiation of microglia. *Front Cell Neurosci* **7**, 45, doi:10.3389/fncel.2013.00045 (2013).

67 Bennett, M. L. *et al.* New tools for studying microglia in the mouse and human CNS. *Proc Natl Acad Sci U S A* **113**, E1738-1746, doi:10.1073/pnas.1525528113 (2016).

68 Harding, S. M. *et al.* Mitotic progression following DNA damage enables pattern recognition within micronuclei. *Nature* **548**, 466-470, doi:10.1038/nature23470 (2017).

69 Gluck, S. *et al.* Innate immune sensing of cytosolic chromatin fragments through cGAS promotes senescence. *Nat Cell Biol* **19**, 1061-1070, doi:10.1038/ncb3586 (2017).

70 Sekine, K., Kubo, K. & Nakajima, K. How does Reelin control neuronal migration and layer formation in the developing mammalian neocortex? *Neurosci Res* **86**, 50-58, doi:10.1016/j.neures.2014.06.004 (2014).

71 Loncle, N., Agromayor, M., Martin-Serrano, J. & Williams, D. W. An ESCRT module is required for neuron pruning. *Sci Rep* **5**, 8461, doi:10.1038/srep08461 (2015).

72 Gong, Y. N. *et al.* ESCRT-III Acts Downstream of MLKL to Regulate Necroptotic Cell Death and Its Consequences. *Cell* **169**, 286-300 e216, doi:10.1016/j.cell.2017.03.020 (2017).

73 Claude-Taupin, A. *et al.* ATG9A protects the plasma membrane from programmed and incidental permeabilization. *Nat Cell Biol* **23**, 846-858, doi:10.1038/s41556-021-00706-w (2021).

74 Martini-Stoica, H., Xu, Y., Ballabio, A. & Zheng, H. The Autophagy-Lysosomal Pathway in Neurodegeneration: A TFEB Perspective. *Trends Neurosci* **39**, 221-234, doi:10.1016/j.tins.2016.02.002 (2016).

75 Pastore, N. *et al.* TFEB and TFE3 cooperate in the regulation of the innate immune response in activated macrophages. *Autophagy* **12**, 1240-1258, doi:10.1080/15548627.2016.1179405 (2016).

76 Ponpuak, M. *et al.* Secretory autophagy. *Curr Opin Cell Biol* **35**, 106-116, doi:10.1016/j.ceb.2015.04.016 (2015).

77 Ejlerskov, P. *et al.* Tubulin polymerization-promoting protein (TPPP/p25alpha) promotes unconventional secretion of alpha-synuclein through exophagy by impairing autophagosome-lysosome fusion. *J Biol Chem* **288**, 17313-17335, doi:10.1074/jbc.M112.401174 (2013).

78 Gui, X. *et al.* Autophagy induction via STING trafficking is a primordial function of the cGAS pathway. *Nature* **567**, 262-266, doi:10.1038/s41586-019-1006-9 (2019).

79 Dupont, N. *et al.* Autophagy-based unconventional secretory pathway for extracellular delivery of IL-1beta. *EMBO J* **30**, 4701-4711, doi:10.1038/emboj.2011.398 (2011).

80 Hayakawa, K. *et al.* Transfer of mitochondria from astrocytes to neurons after stroke. *Nature* **535**, 551-555, doi:10.1038/nature18928 (2016).

81 Joshi, A. U. *et al.* Fragmented mitochondria released from microglia trigger A1 astrocytic response and propagate inflammatory neurodegeneration. *Nat Neurosci* **22**, 1635-1648, doi:10.1038/s41593-019-0486-0 (2019).

82 Budnik, V., Ruiz-Canada, C. & Wendler, F. Extracellular vesicles round off communication in the nervous system. *Nat Rev Neurosci* **17**, 160-172, doi:10.1038/nrn.2015.29 (2016).

83 Asai, H. *et al.* Depletion of microglia and inhibition of exosome synthesis halt tau propagation. *Nat Neurosci* **18**, 1584-1593, doi:10.1038/nn.4132 (2015).

84 Yokoi, A. *et al.* Mechanisms of nuclear content loading to exosomes. *Sci Adv* **5**, eaax8849, doi:10.1126/sciadv.aax8849 (2019).

85 Goldmann, T. *et al.* Origin, fate and dynamics of macrophages at central nervous system interfaces. *Nat Immunol* **17**, 797-805, doi:10.1038/ni.3423 (2016).

86 Utz, S. G. *et al.* Early Fate Defines Microglia and Non-parenchymal Brain Macrophage Development. *Cell* **181**, 557-573 e518, doi:10.1016/j.cell.2020.03.021 (2020).

87 Bialas, A. R. *et al.* Microglia-dependent synapse loss in type I interferon-mediated lupus.

88 Mackenzie, K. J. *et al.* cGAS surveillance of micronuclei links genome instability to innate immunity. *Nature* **548**, 461-465, doi:10.1038/nature23449 (2017)

89 Bialas, A. R. *et al.* Microglia-dependent synapse loss in type I interferon-mediated lupus. *Nature* **546**, 539-543, doi:10.1038/nature22821 (2017).

Figures and legends

A

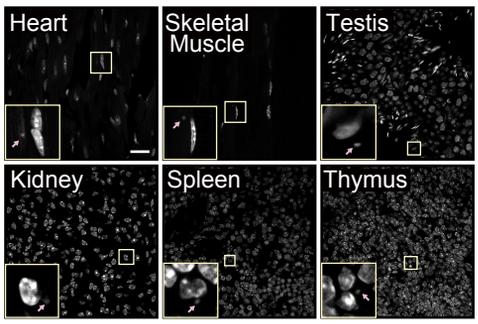

B

Tissues	Sum of total cells	Total # of Nucleus/mm^2 Average	Total # of MNs/ mm^2 Average	% MNs Mean ± SEM
Heart	1335	22.80	0.07	0.29 ± 0.15
Skeletal Muscle	468	8.00	0.02	0.20 ± 0.20
Testis	7563	129.11	1.01	0.74 ± 0.18
Kidney	5699	97.31	1.71	1.74 ± 0.22
Spleen	9731	166.17	2.51	1.51 ± 0.30
Thymus	17611	300.73	0.55	0.16 ± 0.03

MNs; micronuclei, n=6, 3 images/tissue, 2 samples in each tissues, 8 weeks ages

C

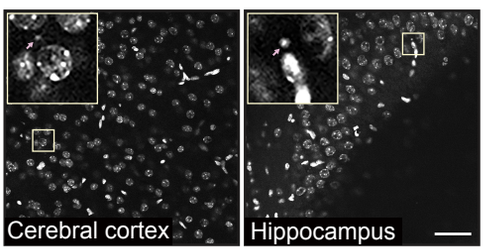

D

Tissues	Sum of total cells	Total # of Nucleus/mm^2 Average	Total # of MNs/ mm^2 Average	% MNs Mean ± SEM
Cerebral cortex	2078	346.3	1.17	0.36 ± 0.12
Hippocampus	1341	223.5	1.33	0.58 ± 0.14

MNs; micronuclei, n=6, 3 images/tissue, 2 samples in each tissues, 8 weeks ages

Figure 1 Micronuclei emerge in various tissues under normal conditions

(A) Nuclei in each tissue (heart, skeletal muscle, testis, kidney, spleen, thymus) from 8 weeks ages mice were stained with Hoechst 33342. Insets show an enlargement of the micronuclei in the boxed area. Arrows indicate micronuclei. Scale bar: 50 μm. (B) The table shows the quantification of micronuclei in Figure 1A by human observers. The small nucleus-like structure, which is approximately less than 2.0 μm, was counted as a micronucleus. The three images were obtained from the tissue sections prepared from a single mouse. The other three images were obtained from an alternate mouse (a total of 6 images from 2 mouse brains). (C) Nuclei in the brain (cerebral cortex and hippocampus) from 2-month-old mice were stained with DAPI. Insets show an enlargement of the micronuclei in the boxed area. Arrows indicate micronuclei. Scale bar: 50 μm. (D) The table shows the quantification of micronuclei in Figure 1C by human observers. The small nucleus-like structure, which is approximately less than 2.0 μm, was counted as a micronucleus. The three images were obtained from the tissue sections prepared from a single mouse. The other three images were obtained from an alternate mouse (a total of 6 images from 2 mouse brains). (A)-(D)The experiments were conducted with Dr. F. Tsuruta. The quantification is conducted with K. Akiyama.

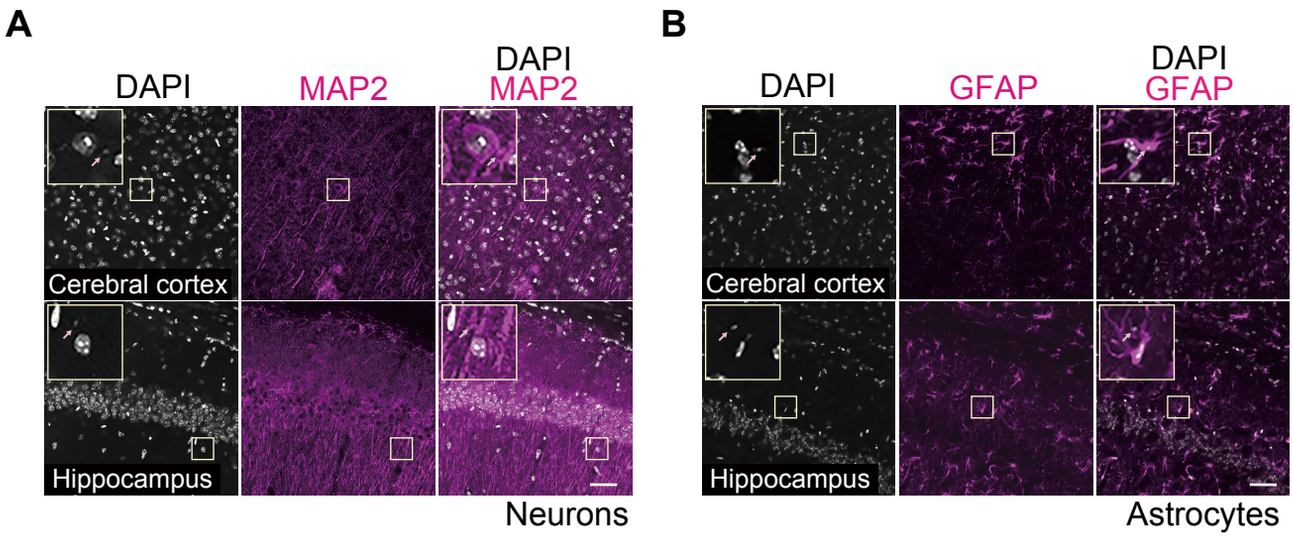

Figure 2 Micronuclei emerge in the brain under normal conditions

(A) Immunostaining of neurons in the cerebral cortex and hippocampus of 2-month-old mice by anti-MAP2 antibody(neuron marker). Insets show an enlargement of the micronuclei in the boxed area. Arrows indicate micronuclei. Scale bar: 50 μm. (B) Immunostaining of astrocyte in the cerebral cortex and hippocampus of 2-month-old mice with an anti-GFAP antibody(astrocyte marker). Insets show an enlargement of the micronuclei in the boxed area. Arrows indicate micronuclei. Scale bar: 50 μm.

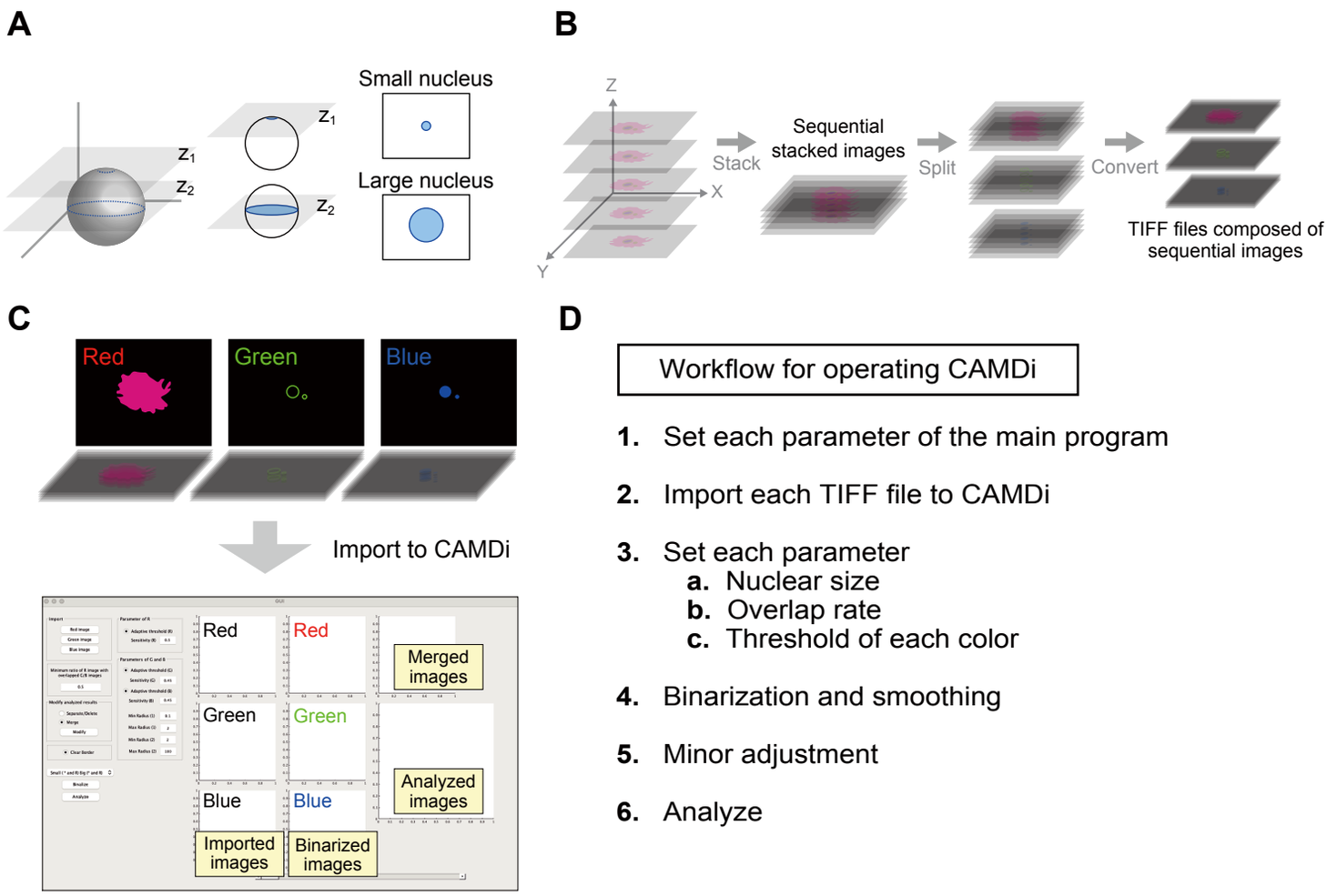

Figure 3 Developing the micronuclei analysis tool using the MATLAB-based program

(A) Schematic illustration of analyzing large and small nuclei. Nuclear size is altered if the images are taken from the different sections (Z_1 and Z_2). Z_1: an upper section, Z_2: a middle section. (B)(C) Images are divided into three different colors (blue, green, and red). Red shows images stained by cell marker. Green and blue show images stained by the nuclear marker. (B) Images need to be adjusted to a suitable format before importing into the CAMDi. Images should be a single or sequential TIFF file. (C) Image processing step for importing data into CAMDi and representative window. Illustrations indicate cell body (red), nuclear envelope (green), and chromatin (blue). (D) Image processing workflow for quantification of micronuclei.

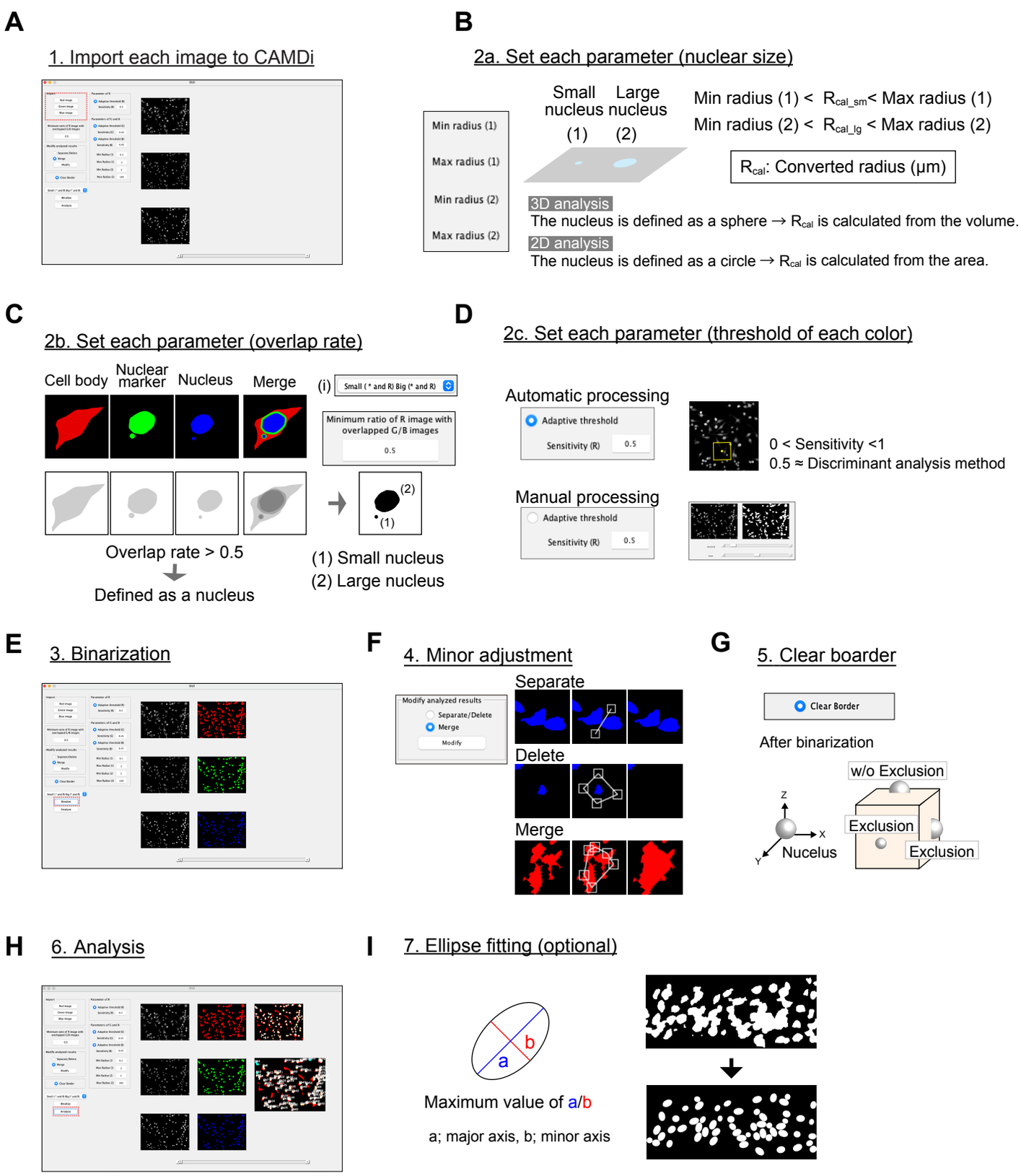

Figure 4 Processing flow of the MATLAB-based program, CAMDi

(A) The TIFF images are imported into CAMDi. (B) Definition of the size of the nucleus, (1) small nucleus, and (2) regular nucleus. (C) Definition of the overlapped rate: the default value is 0.5. Both overlapped areas and non-overlapped areas can be selected using window (i). (D) Definition of the threshold of signals. The discriminant analysis method is applied when automatic processing is selected. (E) Original images are converted into binarized images. (F) Merged or divided signals in the binarized images are corrected. (G) Signals on the border can be eliminated. (H) The diameter of nuclear and the number of nuclei in images can be acquired after analysis. The result data are exported as CSV files. (I) High-density signals are effectively separated using the ellipse fitting function. This function can only be used on the Microsoft Windows platform to date.

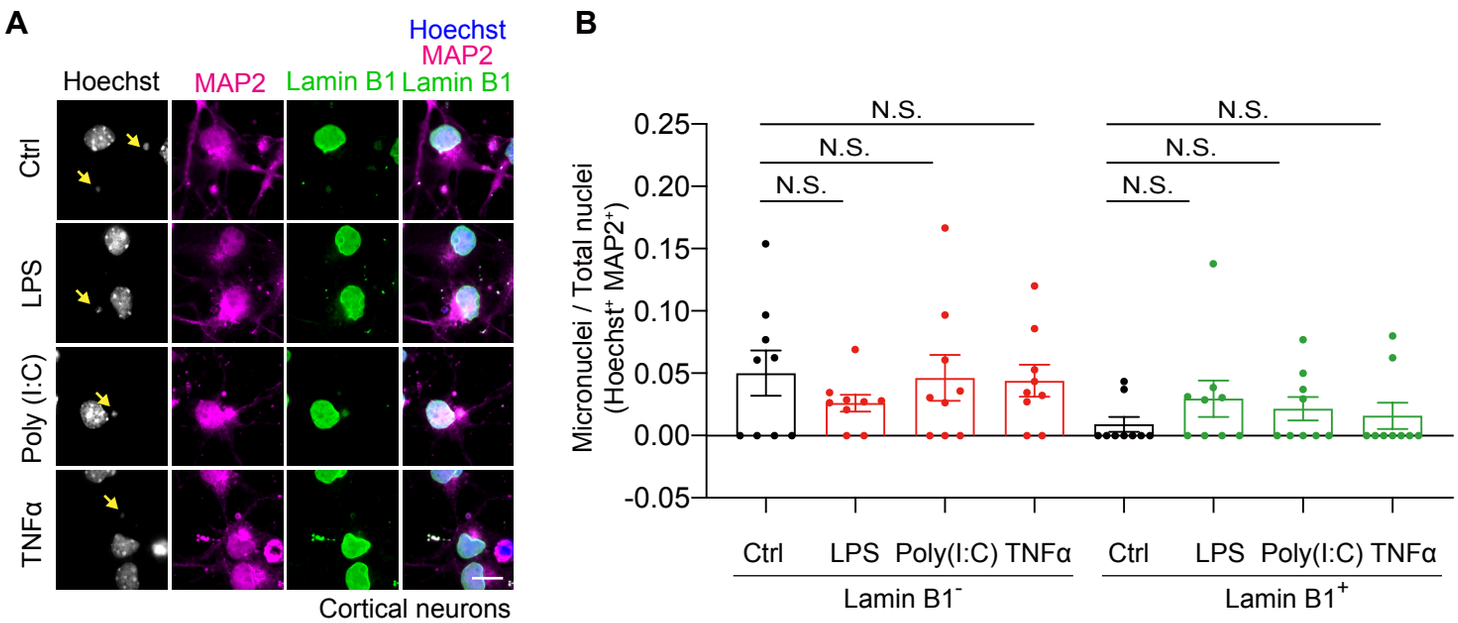

Figure 5 Inflammatory stimulations have little effect on micronuclei formation in neurons *in vitro*
(A) Primary neurons of the cerebral cortex were isolated and plated at 1.0 x 10^6 cells in a 12-well plate, and cultured for 4 days. Immunostaining shows the micronuclei formation in the presence or absence of either 1.0 µg/ml LPS, 5.0 µg/ml Poly (I:C), or 50 ng/ml TNFα for 24 hours. Immunostaining with an anti-lamin b1 antibody(nuclear marker) and an anti-MAP2 antibody(neuron marker). Arrows indicate micronuclei. Scale bar: 10 µm. (B) The graph shows the rate of micronucleus in the primary neurons treated as in (A). Lamin b1 negative (left) and positive micronuclei (right) are counted separately. The small nucleus (less than 1.5 µm) quantified by CMADi is defined as a micronucleus. n=9 field; mean ± standard error of the mean (SEM), N.S. not significant by one-way analysis of variance (ANOVA) Tukey-Kramer statistical tests. The data were reproduced in two independent experiments. (A)(B)The experiments were conducted with Dr. F. Tsuruta.

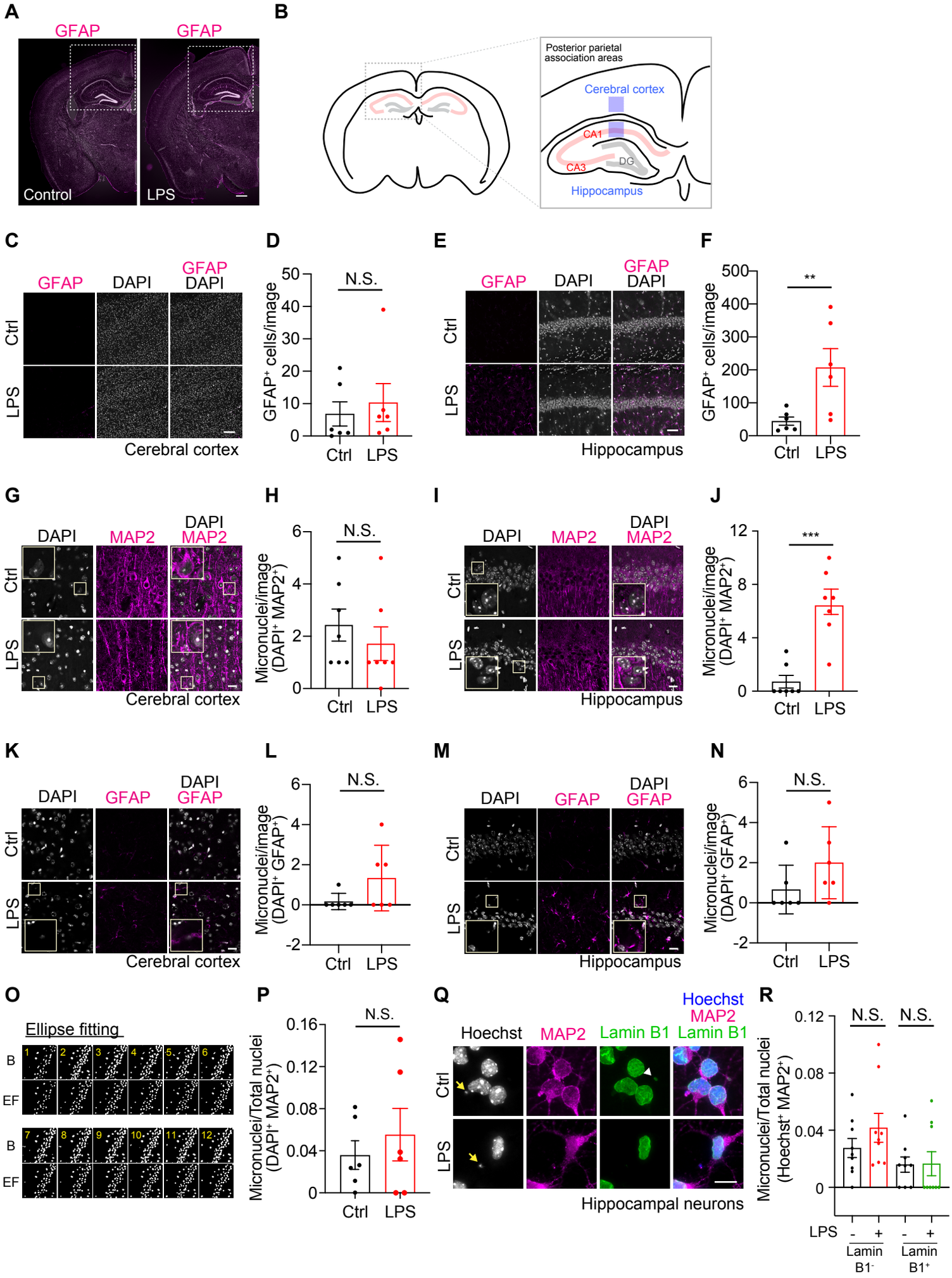

Figure 6 Inflammatory stimulation promotes micronuclei formation in neurons

Figure 6 Inflammatory stimulation promotes micronuclei formation in neurons

(A) Immunostaining with an anti-GFAP antibody(astrocyte marker) in the brain section of 2-month-old mice with or without 1.0 μg/kg LPS for 24 hours. Insets indicate the quantified areas. Scale bar: 500 μm. (B) The quantified areas in Fig5C to 5P are illustrated as blue boxes. (C) Immunostaining with an anti-GFAP antibody(astrocyte marker) in the cerebral cortex of 2-month-old mice with or without 1.0 μg/kg LPS for 24 hours. Scale bar: 50 μm. (D) The graph shows the population of GFAP-positive astrocytes. n=6, $1.02x10^5$ μm^2/image; 6 images obtained from 2 independent mouse brains; mean ± SEM, N.S. not significant by Student's *t*-test. (E) Immunostaining with an anti-GFAP antibody(astrocyte marker) in the hippocampus of 2-month-old mice with or without 1.0 μg/kg LPS for 24 hours. Scale bar: 50 μm. (F) The graph shows the number of GFAP-positive astrocytes. n=6, $1.02x10^5$ μm^2/image, 6 images obtained from 2 independent mouse brains; mean ± SEM, $^{**}p<0.01$ by Student's *t*-test. (D)(F)The quantification was conducted with R. Tsuchiya(a second-year master's student) (G) Immunostaining with an anti-MAP2 antibody(neuron marker) showing micronuclei in the cerebral cortex of 2-month-old mice with or without 1.0 μg/kg LPS for 24 hours. Scale bar: 20 μm. (H) The graph shows the number of micronuclei in neurons per image. The small nucleus (less than 2.5 μm) quantified by CMADi was defined as a micronucleus. n=6, $2.56x10^4$ μm^2/image, 7 images obtained from 2 independent mouse brains; mean ± SEM, N.S. not significant by Student's *t*-test. (I) Immunostaining with an anti-MAP2 antibody(neuron marker) showing the micronuclei in the hippocampus of 2-month-old mice with or without 1.0 μg/kg LPS for 24 hours. Scale bar: 20 μm. (J) The graph shows the number of micronuclei in neurons per image of the CA1 region. The small nucleus (less than 2.5 μm) quantified by CMADi was defined as a micronucleus. n=6, $2.56x10^4$ μm^2/image, 7 images obtained from 2 independent mouse brains; mean ± SEM, $^{***}p<0.005$ by Student's *t*-test. (K) Immunostaining with an anti-GFAP antibody(astrocyte marker) showing micronuclei in the cerebral cortex of 2-month-old mice with or without 1.0 μg/kg LPS for 24 hours. Scale bar: 20 μm. (L) The graph shows the number of micronuclei in astrocytes per image. The small nucleus (less than 2.0 μm) quantified by CMADi was defined as a micronucleus. n=6, $2.56x10^4$ μm^2/image, 6 images obtained from 2 independent mouse brains; mean ± SEM, N.S. not significant by Student's *t*-test. (M) Immunostaining with an anti-GFAP antibody(astrocyte marker) showing the micronuclei in the hippocampus of 2-month-old mice with or without 1.0 μg/kg LPS for 24 hours. Scale bar: 20 μm. (N) The graph shows the number of micronuclei in astrocytes per image in the CA1 region. The small nucleus (less than 2.0 μm) quantified by CMADi was defined as a micronucleus. n=6, $2.56x10^4$ μm^2/image, 6 images obtained from 2 independent mouse brain; mean ± SEM, $^{***}p<0.005$ by Student's *t*-test.(O) Representative sequential images of the hippocampus stained with DAPI before and after operating the ellipse fitting. B: binarized images before operating ellipse fitting, EF: converted images after ellipse fitting. (P) The graph shows the population of micronuclei in $MAP2^+$ neurons per image. 6 images were obtained from 2 independent mouse brains, $2.56x10^4$ μm^2/image; mean ± SEM, N.S. not significant by Student's *t*-test. (Q) The primary hippocampal neurons were isolated and plated at 1.0 x 10^6 cells in a 12-well plate and cultured for 4 days. Immunostaining with an anti-MAP2 antibody(neuron marker) and Lamin b1 antibody(nuclear marker) showed the micronuclei formation in the presence or absence of 1.0 μg/ml LPS for 24 hours. Arrows indicate micronuclei. Scale bar: 10 μm. (R) The graph shows the number of micronuclei-positive neurons. The small nucleus (less than 1.5 μm) quantified by CAMDi was defined as a micronucleus. n=9 field; mean ± SEM, N.S. not significant by one-way ANOVA Tukey-Kramer statistical tests. Data were reproduced in two independent experiments. (Q)(R)The experiments were conducted with Dr. F. Tsuruta.

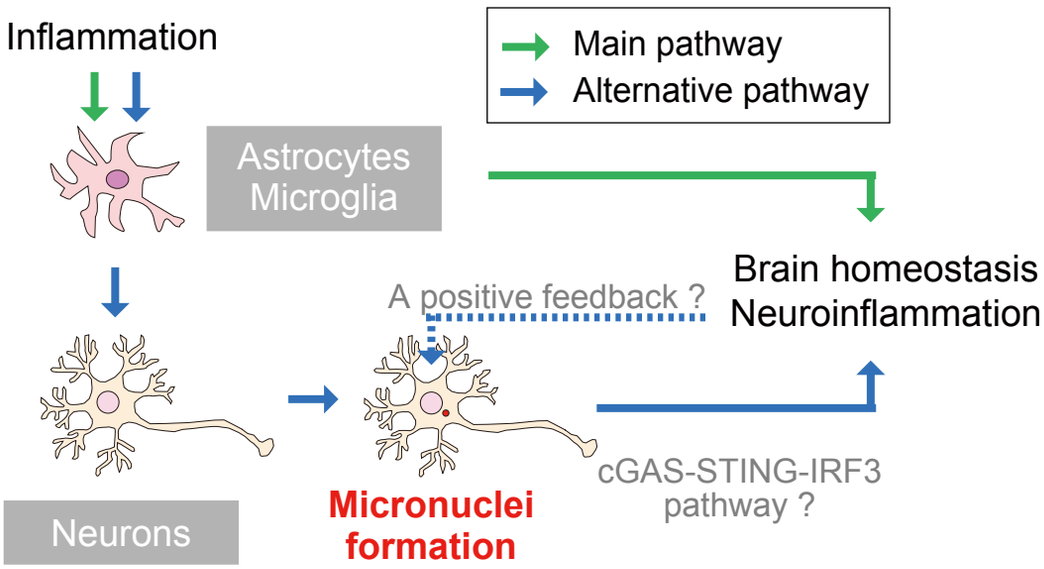

Figure 7 A model describing the pathway linking neuroinflammation to micronuclei formation
The inflammatory stimulations activate glial cells and promote neuroinflammation as the main pathway. The neuroinflammation further increases the micronuclei formation in the neurons and this may form an alternative malignant cycle. Since micronuclei can activate the cGAS-STING pathway, micronuclei induced by the inflammatory response may act as a positive feedback pathway.

Table 1 Setting Initial parameters of MATLAB program

A. Set basic parameters of the main program (file: main.m) in CAMDi

prm.dim_cell_analyze = X;	**Cell analyze (X)**; two-dimensional image, X -> 2; three-dimentional image, X -> 3
prm.dim_cell_radius = X;	**Radius (X)**; Calculate from maximum area, X -> 2; Calculated from maximum volumn, X -> 3
prm.VoxelSpacing = [X Y Z];	**Set scale (X, Y, Y)**; Distance in voxels (unit of length:1 μm)
prm.flag_insertNumber_outputImage = X;	**Numbers (X)**; Show numbers in the binalized image, X -> 1, Don't show numbers, X -> 0
prm.r_area_min = X;	**Radius (X)**; Minimun radius of nucleus (R), unit [μm]
prm.r_area_max = X;	**Radius (X)**; Maximum radius of nucleus (R), unit [μm]
prm3.rate_cover_r_min = X;	**Overlap rate (X)**; Overlap rate between R and G/B, Regular value, X -> 0.5

B. Noise reduction parameters of the main program, each color (file: main.m) in CAMDi

prm.smoothing.degreeOfSmoothing = X;	**Maximum variance of pixel values in the smoothing area (X)**; Smoothing (R) off, X -> 0
prm.smoothing.spatialSigma = X;	**Standard deviation of spatial radius in the smoothing area (X)**; Smoothing (R) off, X -> 0
prm.morphology.w1 = X;	**Molphology scaling size for the area reconnection (X)**; Don't reconnection (R) , X -> 0
prm.morphology.w2 = X;	**Molphology scaling size for the noize reduction (X)**; Don't noise reduction (R) , X -> 0
prm2.smoothing.degreeOfSmoothing = X;	**Maximum variance of pixel values in the smoothing area (X)**; Smoothing (G) off , X -> 0
prm2.smoothing.spatialSigma = X;	**Standard deviation of spatial radius in the smoothing area (X)**; Smoothing (G) off, X -> 0
prm2.morphology.w1 = X;	**Molphology scaling size for the area reconnection (X)**; Don't reconnection (G), X -> 0
prm2.morphology.w2 = X;	**Molphology scaling size for the noize reduction (X)**; Don't noise reduction (G), X -> 0
prm22.smoothing.degreeOfSmoothing = X;	**Maximum variance of pixel values in the smoothing area (X)**; Smoothing (B) off, X -> 0
prm22.smoothing.spatialSigma = X;	**Standard deviation of spatial radius in the smoothing area (X)**; Smoothing (B) off, X -> 0
prm22.morphology.w1 = X;	**Molphology scaling size for the area reconnection (X)**; Don't reconnection (B), X -> 0
prm22.morphology.w2 = X;	**Molphology scaling size for the noize reduction (X)**; Don't noise reduction (B), X -> 0

C. Set ellipse fitting parameters of the main program, each color (file: main.m) in CAMDi

prm.FittingEllipse = X;	**Maximum ratio of major/minor axis (X)**; The major/minor axis (R), off, X -> 0, circle X -> 1, ellipse-> >1
prm2.FittingEllipse = X;	**Maximum ratio of major/minor axis (X)**; The major/minor axis (G), off, X -> 0, circle X -> 1, ellipse-> >1
prm22.FittingEllipse = X;	**Maximum ratio of major/minor axis (X)**; The major/minor axis (B), off, X -> 0, circle X -> 1, ellipse-> >1

Programming in collaboration with Dr. T. Nagata.